Effect of annealing temperature on structural, morphological and dielectric properties of La$_{0.8}$Ba$_{0.1}$Ce$_{0.1}$FeO$_3$ perovskite

E. M. Benali[1,2,3], A. Benali[1,2,3,*] , M. Bejar[2], E. Dhahri[2], M. P. F. Graca[3], M. A. Valente[3], P. Sanguino[4], and B. F. O. Costa[1]

[1] Physics Department, CFisUC, University of Coimbra, Rua Larga, 3004-516 Coimbra, Portugal

[2] Laboratoire de Physique Appliquée, Faculté Des Sciences, Université de Sfax, B.P. 1171, 3000 Sfax, Tunisie

[3] I3N and Physics Department, University of Aveiro, 3810-193 Aveiro, Portugal

[4] CEMMPRE, Mechanical Engineering Department, University of Coimbra, Rua Luís Reis Santos, 3030-788 Coimbra, Portugal

ABSTRACT

The La$_{0.8}$Ba$_{0.1}$Ce$_{0.1}$FeO$_3$ compounds were prepared by the auto-combustion route and annealed at two different temperatures to study their effect on the structural, morphological and dielectric properties of the Barium- and Cerium-substituted LaFeO$_3$ compound. The X-ray diffraction analysis revealed that both compounds crystallized in the orthorhombic structure belonging to the *Pnma* space group. The rise of the annealing temperature from 700 to 900 °C was found to lead to the increase of the average grain size value as characterized by SEM. Furthermore, two clear relaxations phenomena have been detected using the Nyquist and Argand's plots of dielectric impedance and Modulus curves at different temperatures, which are attributed to both grain and grain boundary contributions. Their activation energies have been calculated not only from the frequency dependence of both imaginary parts of impedance (Z'') and modulus (M'') but also from the contribution of the resistances deduced from the Nyquist plots. These plots have been adjusted using two circuits in series, each of which containing a resistance in parallel to a CEP capacitance. The conduction mechanism was analyzed by ac conduction using the Jonscher's power law. The NSPT conduction model has been confirmed for both compounds in which the rise in heat treatment decreases the binding energy of carriers.

Address correspondence to E-mail: benaliadel96@gmail.com

1 Introduction

The perovskite oxides with ABO_3 structure, in which the A-site cation is a rare-earth element and the B-site is a transition metal (Cr, Mn, Fe, Co, etc.), have been the most studied oxides as potential candidates for various applications over the past few years [1–5]. These perovskites, with 'La' in position A and 'Fe' in B position, are called the lanthanum orthoferrites "$LaFeO_3$" (LFO_3), which present an orthorhombically distorted perovskite structure (*Pnma* space group). These lanthanum orthoferrites are known as an antiferromagnetic (AFM) metals with a high ordering temperature $T_N \sim 740$ K [6]. Think to their different physical properties, they are used for a long time ago in many applications: magnetic materials [7], a novel sensing material for detecting toxic gases [8], as oxide fuel cells [9], batteries [10] and as catalytic materials [11]. Recently, according to a great number of researchers, the lanthanum orthoferrites compounds were synthetized by different methods, such as Sol–Gel [12]; co-precipitation [13]; hydrothermal [14]; the auto-combustion of citrate and nitrates process [15] and the Solid-State reaction [16].

It has been shown that the substitution in A and B sites in LFO_3 systems by a transition metal, with general structure $La_{(1-x)}A_{(x)}FeO_3$ and $LaFe_{(1-x)}B_{(x)}O_3$, enhanced their properties [17, 18]. Earlier studies showed that the insertion of "Ba'' ion in the A-site of the LFO_3 [19] compound improved his response to ethanol gas. Moreover, Xiang et al. [20] have confirmed that the activity of the Lanthanum Ferrite perovskite is strongly improved by the insertion of the Cerium in the A-site. They have also proven that the CeO_2 secondary phase is generated when the amount of Ce ions exceeds a value of 10%. Furthermore, they have demonstrated that the appropriate amount of substitution of Lanthanum ions is almost equal to 20% and that in the case of double substitutions in A-site, an amount of 10% for each inserted ion enhances the physico-chemical properties of the multi substituted lanthanum ferrite LFO_3 compounds [21–23]. In our previous research work, we have studied the effect of synthesis method on the physico-chemical properties of the $La_{0.8}Ba_{0.1}Ce_{0.1}FeO_3$ compound and concluded that the best properties have been found when using the auto-combustion method [24].

The present paper is interested in the study of the effect of the annealing temperature on the structural, morphological and dielectric properties of $La_{0.8}Ba_{0.1}Ce_{0.1}FeO_3$ compound prepared by the auto-combustion method.

2 Experimental

The $La_{0.8}Ba_{0.1}Ce_{0.1}FeO_3$ compound was prepared by the auto-combustion route using the glycine [25]. According to this method, the corresponding amounts of Lanthanum nitrate $La(NO_3)_3 \cdot 6H_2O$; Barium nitrate $Ba(NO_3)_2$; Cerium nitrate $Ce(NO_3)_3 \cdot 6H_2O$ and ferric nitrate $Fe(NO_3)_3 \cdot 9H_2O$ are dissolved in distilled water. The obtained solution was kept under magnetic stirring, at room temperature until obtaining a transparent solution. Then, the glycine was added to the mixture as a chelating agent and the temperature was raised to 90 °C till the formation of a viscos gel. After that, the self-combustion took place giving birth to a black powder. This powder was pressed into pellets and sintered at 700 °C. To study the effect of the annealing temperature on the different properties, the pellets were then annealed at 900 °C.

The structure of our two samples annealed at 700 and 900 °C was studied using the X-Ray Diffraction (XRD). The measurements were realized at room temperature using Cu-Kα with step size of 0.022497° in the range of 2 θ = 18° to 80°. The microstructure of our two samples was carried out using a VEGA3 TESCAN scanning electron microscope (SEM). For the dielectric measurements, the two samples were placed between two electrodes, in a range of temperatures between 140 and 400 K. The impedance was measured between 100 Hz and 1 MHz using an Agilent 4294 A Precision impedance analyzer, in the C_P–R_P configuration.

3 Results and discussion

3.1 Structural and morphological properties

The X-ray diffraction (XRD) patterns of LBCFO-700 and LBCFO-900 compounds plotted in Fig. 1 were compared to the XRD diffractogram determined in the case of the $La_{0.8}Ba_{0.1}Bi_{0.1}FeO_3$ sample of our previous work [24] to confirm the phase structure of the prepared samples. As can be clearly seen, the XRD of
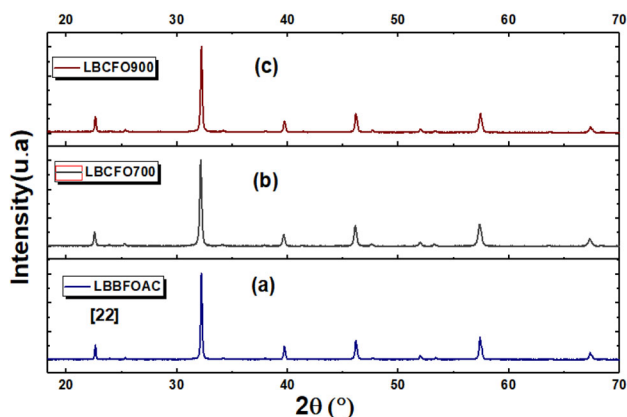
Fig. 1 Room temperature XRD patters of our samples **a** LBBFOAC (La$_{0.8}$Ba$_{0.1}$Bi$_{0.1}$FeO$_3$ prepared with the auto-combustion route), **b** LBCFO-700 and **c** LBCFO-900

all presented compounds revealed the same reflection peaks, indicating the good crystallinity and confirming the ability of the auto-combustion preparation method, with both heat treatment temperatures, to produce pure phases with high crystallinity. The obtained XRD were subjected to Rietveld analysis using FULLPROF software [26] and the results of the refinement are shown in Fig. 2a, b. The reflection peaks of both samples are assigned to the orthorhombic structure with *Pnma* space group pertaining to the results of the previously studied compound LaFeO$_3$ [27]. The structural refinement allows us to draw the graphical model of both samples with *Pnma* space group (Fig. 2a, b). The unit cell with the FeO6 octahedra of both compounds have been drawn using the Vesta software and shown in Fig. 2a′, b′. As one can see, the structure of both LBCFO-700 and LBCFO-900 compounds is a composed by tilted and deformed corner-sharing FeO$_6$ octahedra (Fe ions occupied the center while Oxygen ions occupied the six vertices of the octahedra) with larger A cations filling the cavities between eight FeO$_6$ octahedra. The Refined structural parameters are collected in Table 2. The both Fe–O bond lengths were found to be around 1.99 Å and 2.15 Å for LBBCFO-700 compound and 1.97 Å, 2.06 Å for LBBCFO-900 compound, which are in good agreement with the previous work [28]. The bond angles Fe–O$_1$–Fe and Fe–O$_2$–Fe increase with the increase of the sintering temperature indicated a decrease in the octahedral rotations [29] (Table 1).

On the other hand, the average crystallite size was calculated using the Williamson–Hall formula illustrated by the following equation [30]:

$$\beta \cos(\theta) = \frac{K \times \lambda}{D_{W-H}} + 4\varepsilon \times \sin(\theta) \qquad (1)$$

where D_{W-H} is the average crystallites size, ε is the effective strain and θ is the diffraction angle for each peak. Also, $K = 0.9$ is the shape factor, λ is the X-ray wavelength (equal to 1.5405 Å for Cu-Kα radiation), and β is the full width at half maximum. Following the W–H method, the variation of ($\beta \times \cos(\theta)$) vs. ($4 \times \sin(\theta)$) was presented and the D_{W-H} was calculated from the intercept values of a linear adjustment of these two curves (Fig. 2c). The crystallite size values of both compounds were found to be 59.25 nm and 77.09 nm for the LBCFO-700 and LBCFO-900, respectively, are collected in Table 2. It can be noted that the crystallites size of our samples grows when raising the annealing temperature. The crystallites sizes of both compounds. Accordingly, the nanosize criteria for both samples were confirmed.

The surface morphologies of the LBCFO-700 and LBCFO-900 nanoparticles were investigated by the scanning electron microscope (SEM). As can be observed in Fig. 3a, b, the SEM images of both samples showed different shapes (spherical and polygonal) which depends on the increase of the annealing temperature. Furthermore, to interpret the elemental compositions of our samples, we used the X-Ray Dispersive Energy (EDX) (Fig. 3). In the spectrum of EDX for both compounds, the presence of characteristic peaks of La, Ba, Ce, Fe, and O is evidently noticed. Indeed, Fig. 3 reveals the presence of all initial elements, confirming that no loss of any element occurred during the reactions without the existence of any impurity elements. Furthermore, the mapping analyses corroborated a homogeneous distribution of all chemical elements throughout the compound surface. The grain size has been performed on TEM images using image-J software as shown in Fig. 4. According to a Lorentzian adjustment of the grain size distributions, the grain size (D_{TEM}) are found around 107 nm and 173 nm for LBCFO-700 and LBCFO-900 compounds, respectively. For both compounds, the D_{TEM} values are almost 2 times higher than those of crystallites size, which can be explained by the fact that a grain is composed of more than one crystallite.

Fig. 2 a and **b** Rietveld refinement plots of the LBCFO-700 and LBCFO-900 compounds, respectively. **a′** and **b′** the three-dimensional unit cell with the FeO_6 octahedra of the same compounds. **c** Williamson–Hall plots of the studied compounds
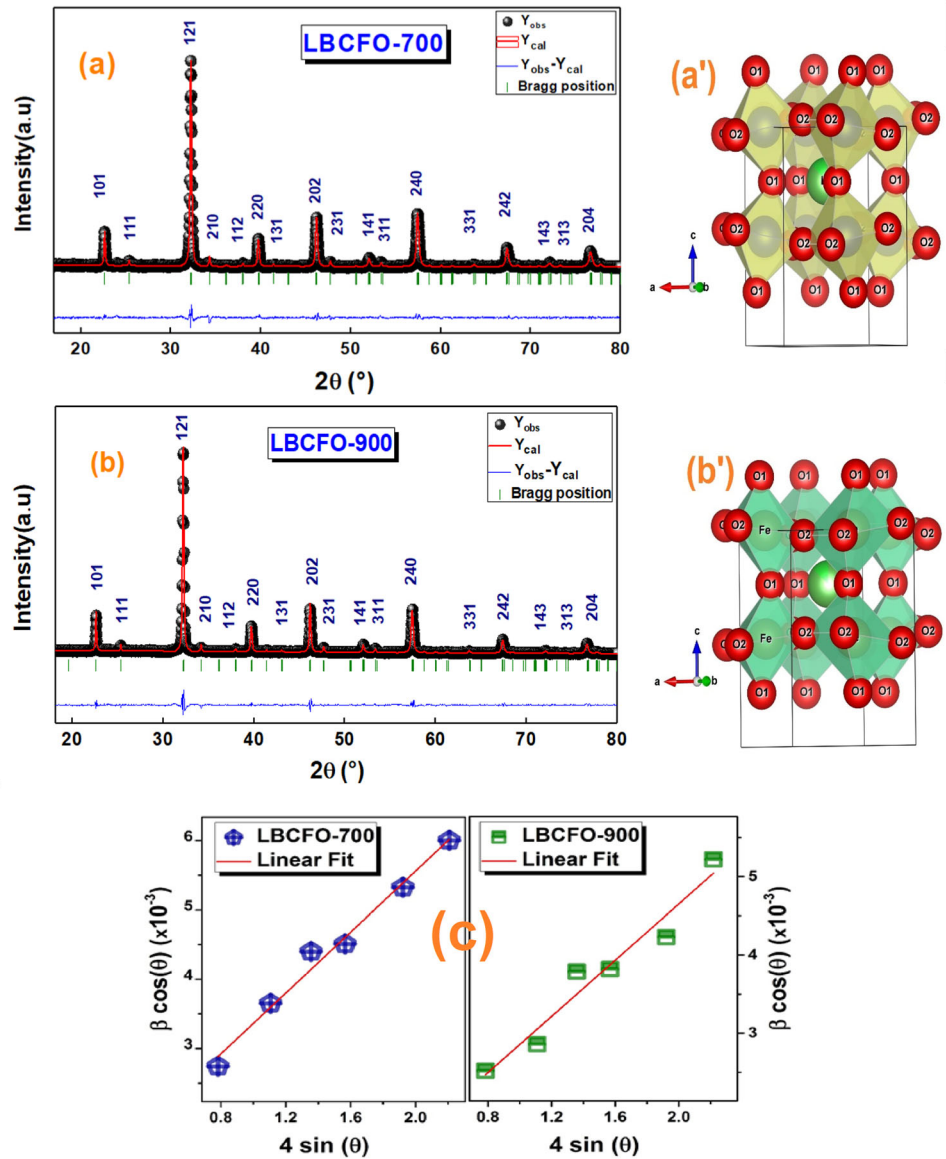

Table 1 Cell parameters of our two compounds: LBCFO-700 and LBCFO-900

	LBCFO-700	LBCFO-900
Space group	*Pnma*	*Pnma*
a (Å)	5.539	5.542
b (Å)	7.860	7.865
c (Å)	5.557	5.558
V (Å^3)	241.93	242.21
χ^2	1.967	2.017
Fe–O$_1$ (Å)	1.995	1.974
Fe–O$_2$ (Å)	2.154	2.066
Fe–O$_1$–Fe (°)	159.363	168.237
Fe–O$_2$–Fe (°)	1151.689	155.410

Table 2 Average crystallite size determined using the Williamson–Hall's method (W–H) and Grain size determined using SEM pictures of LBCFO-700 and LBCFO-900 compounds

	Crystallites size (D_{W-H}) (nm)	Grains size (D_{TEM}) (nm)
LBCFO-700	59.250	107.052
LBCFO-900	77.091	173.640

As compared to our previous work [24], the particle size decreases as consequence of the insertion of Cerium ions in A-site instead of Bismuth ones which is related not only to the ionic radius of these two
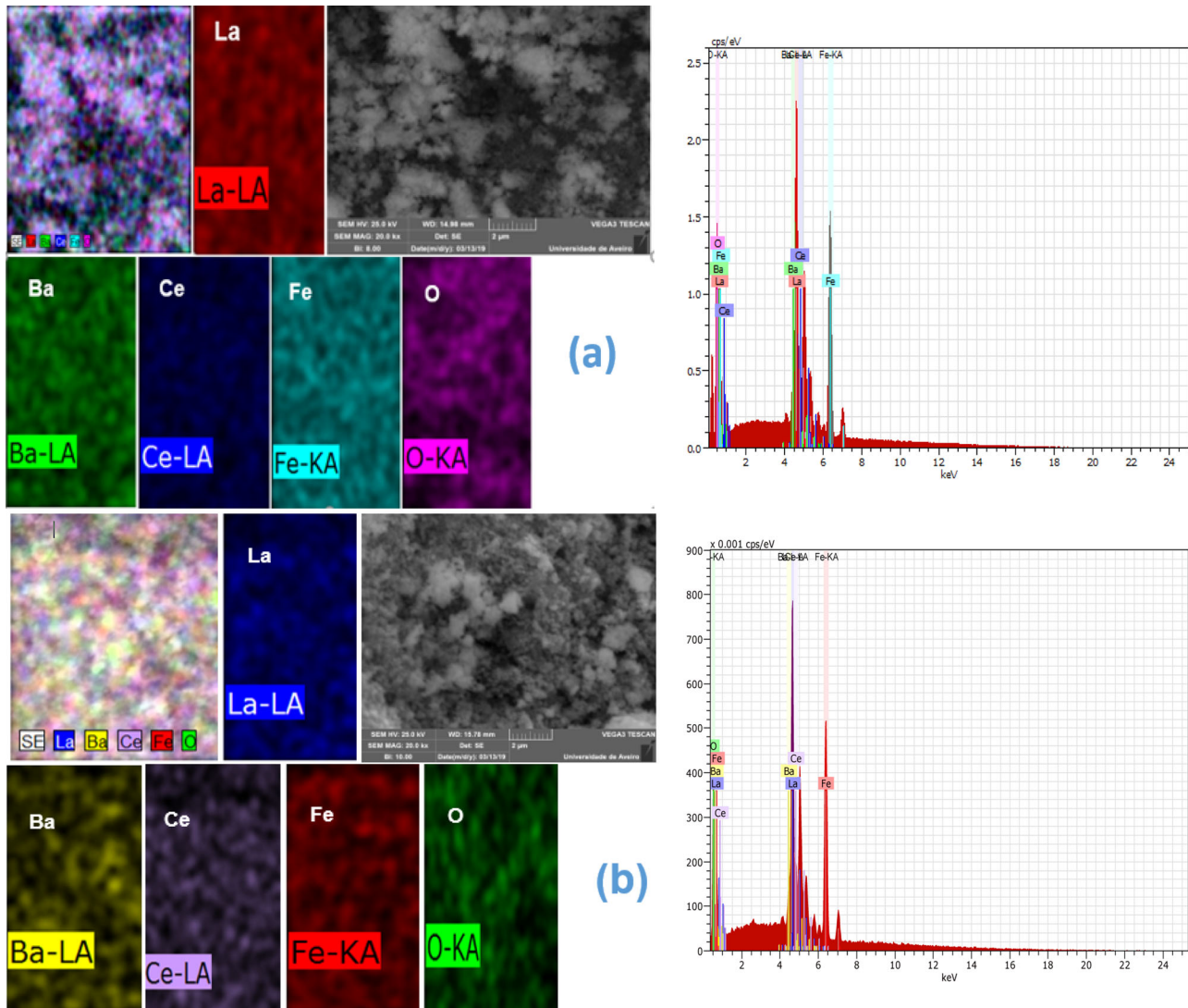
Fig. 3 SEM images and EDX spectrum of the studied compounds: **a** LBCFO-700 and **b** LBCFO-900

ions but also to the change in Iron states concentrations which influence the tilted octahedron FeO_6.

3.2 Impedance analysis

Figure 5a, b shows the variation of the real part of impedance (Z') as a function of the frequency of LBCFO-700 and LBCFO-900 compounds, respectively, at selected temperatures. It is observed that the real part values are higher in the low-frequency range. It was also found that Z', whose value decreased with the increase in temperature, is temperature-dependent, indicating the increase of conductivity [31]. It is worthy to note that, from a certain frequency, the variation of (Z') becomes almost frequency independent with a merge of all Z' curves

due to the release of space charge promoted by a lowering in the barrier properties of the nanomaterials [32]. Importantly, it is obviously seen that the value of the real part of impedance decreases with the increase in the annealing temperature from 700 to 900 °C, which spotlights a decrease in the electrical resistance, and thus an enhancement of conductivity.

In Fig. 5c, d, the imaginary part of the impedance (Z'') for both samples are plotted as a function of the frequency at the temperature range between 260 and 360 K. Both compounds set forth that the Z'' values increase with the increase of frequency, reaching a maximum peak (Z''_{max}) at a characteristic frequency called relaxation frequency [33] Afterward, they decreased for further frequency rising, indicating the presence of a relaxation phenomenon in the

Fig. 4 TEM images and particles size distribution of our compounds **a** LBCFO-700 and **b** LBCFO-900
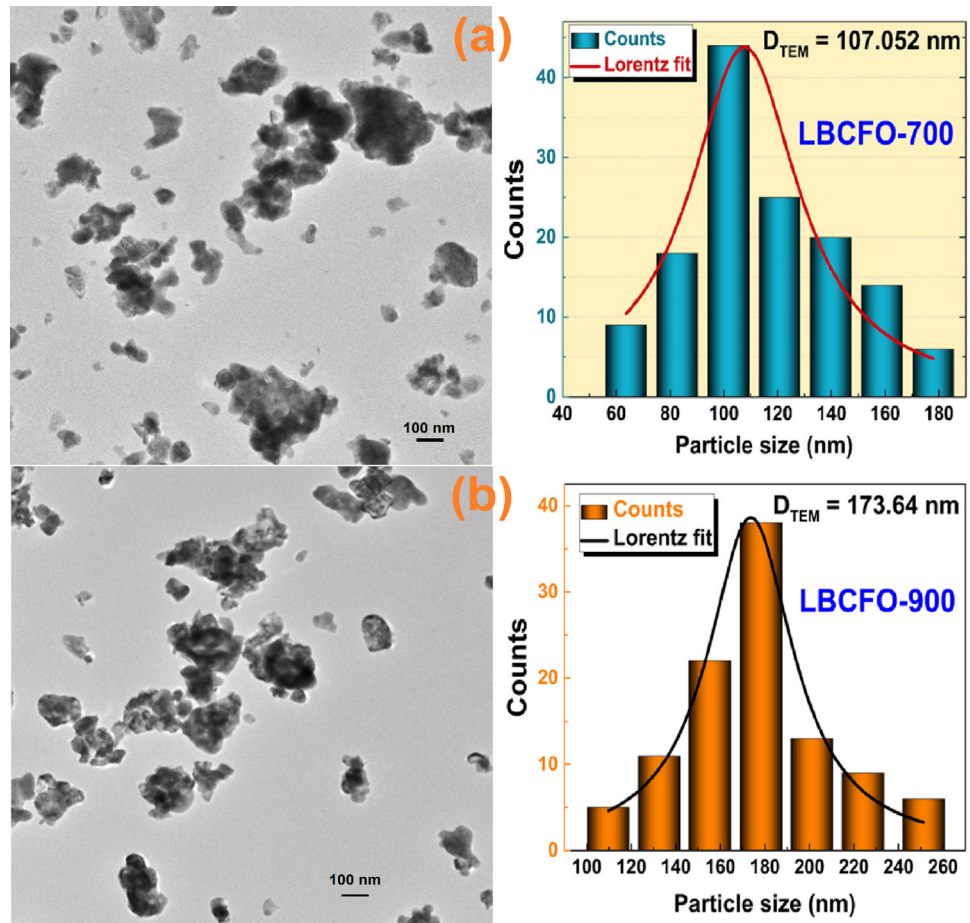
synthesized samples [34]. Besides, the Z'' peaks of both samples are proven to shift to a higher frequency range with the increase in temperature, which affirms the presence of a thermally activated process in the materials. To calculate the activation energy, the temperature dependence of the relaxation frequency for each compound was plotted according to the Arrhenius law expressed as follows:

$$f_{max} = f_0 \exp\left(-\frac{E_a}{k_B \times T}\right) \qquad (2)$$

where f_0 the pre-exponential term, E_a the activation energy and k_B Boltzmann constant. The logarithmic variation of the f_{max} is plotted as a function of $1000/T$ in Fig. 5e. Using the slope of the well-fitting curves, the obtained values of the activation energy were found to be around 0.273 eV for LBCFO-700 and 0.258 eV for LBCFO-900. It can be concluded that the rise in the sintering temperature decrease the activation energy. For both compounds, the activation energy was found to be very close to the needed activation energy for the electron hopping between

Iron states known as the polaronic relaxation which required around 0.26 eV to be achieved [35]. Thus, it is deduced that the relaxation process in the studied compounds is of a polaronic type that acquired between Iron states. We found previously the same relaxation type for $La_{0.8}Ba_{0.1}Bi_{0.1}FeO_3$ compound [24] with a higher activation energy value which confirms again the effect of the nanosize criteria on the dielectric relaxation process.

On another hand, the Nyquist diagrams of the complex impedance (Z'' versus Z') are plotted in Fig. 6a, b at selected temperatures for both samples. The dielectric properties of multi-doped Lanthanum ferrites have been previously reported [21], confirming the presence of more than one contribution from the modulus analysis as well as from the adjustment of the impedance Nyquist plots. It has also been reported that most of the ferrite materials show a non-Debye-type relaxation, generally characterized by asymmetric or small depressed semicircles, whose centers are found to be below the real axis. According to the material nature and type and within a selected

Fig. 5 a, **b** Frequency dependence of the real (Z') part and **c**, **d** the variation of imaginary part (Z'') of the impedance as a function of the frequency at selected temperatures of the LBCFO-700 and LBCFO-900 compounds. **e** The logarithmic variation of the f_{max} as a function of $1000/T$ for both studied compounds
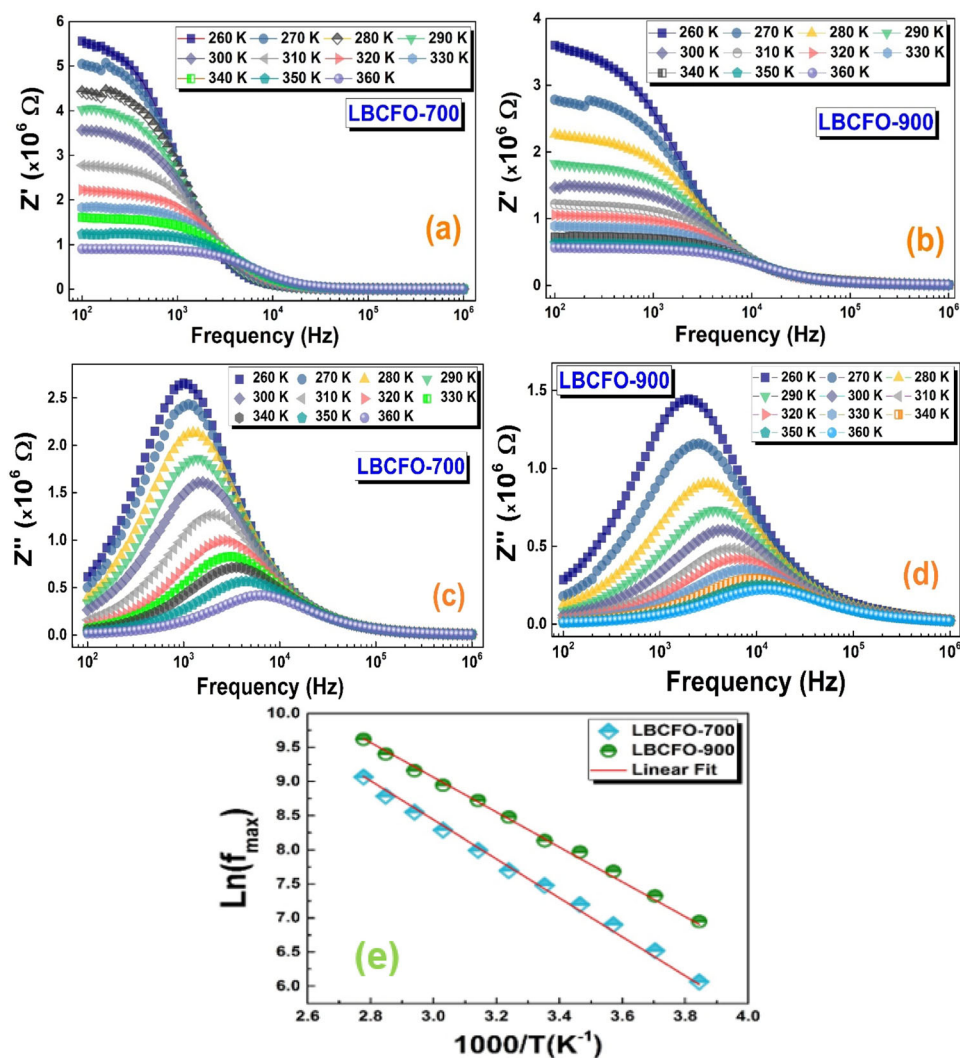

temperature and frequency regions, the Nyquist plots may consist of arcs, spikes or overlapped semicircles or a combination of more than one of them [36]. From a first analysis of these Nyquist plots, it can be deduced that the heat treatment reduces the electrical resistance as shown from the Z'' curves. A clear depressed semi-circle can be seen at low-frequency range, while the existence possibility of another contribution would be confirmed from the adjustment of the Nyquist plots using the Z-view software [37]. The Nyquist plots were fitted by the most adequate electrical equivalent circuits, containing two parallel combinations of R and CPE elements, which are connected in series. While the first one corresponds to grain contribution at higher frequencies, the second corresponds to the grain boundary one at low-frequency range.

The behavior of both contributions would be used to describe the relaxation phenomenon of the synthesized compounds at the indication temperature range.

From the results of the experimental fit of the Nyquist curves, the parameters R_g, R_{gb}, CPE$_g$, CPE$_{gb}, \alpha_g$ and α_{gb} are obtained and summarized in Table 3(a) and (b). For both compounds, we can deduce that the resistance values of the boundaries grains and grains decrease with the rise of temperature, which is due to the increase of the mobility of charges carriers or the decrease of the average potential barriers energies. This behavior was reported to be a characteristic of p-type semiconductor material [38]. Importantly, we reported a reduced electric resistance for both compounds as compared to the pure and to the doped LaFeO3 bulk compound [39–41] which allow as to conclude the advantage of

Fig. 6 Nyquist plot at selected temperatures and equivalent circuit of the **a** LBCFO-700 and **b** LBCFO-900 samples. **c** the adjustment results for both compounds at 350 K with the used equivalent circuit. **d** The Arrhenius plots of the resistances of grain (R_g) and grain boundary (R_{gb}) versus $10^3/T$ of the both compounds
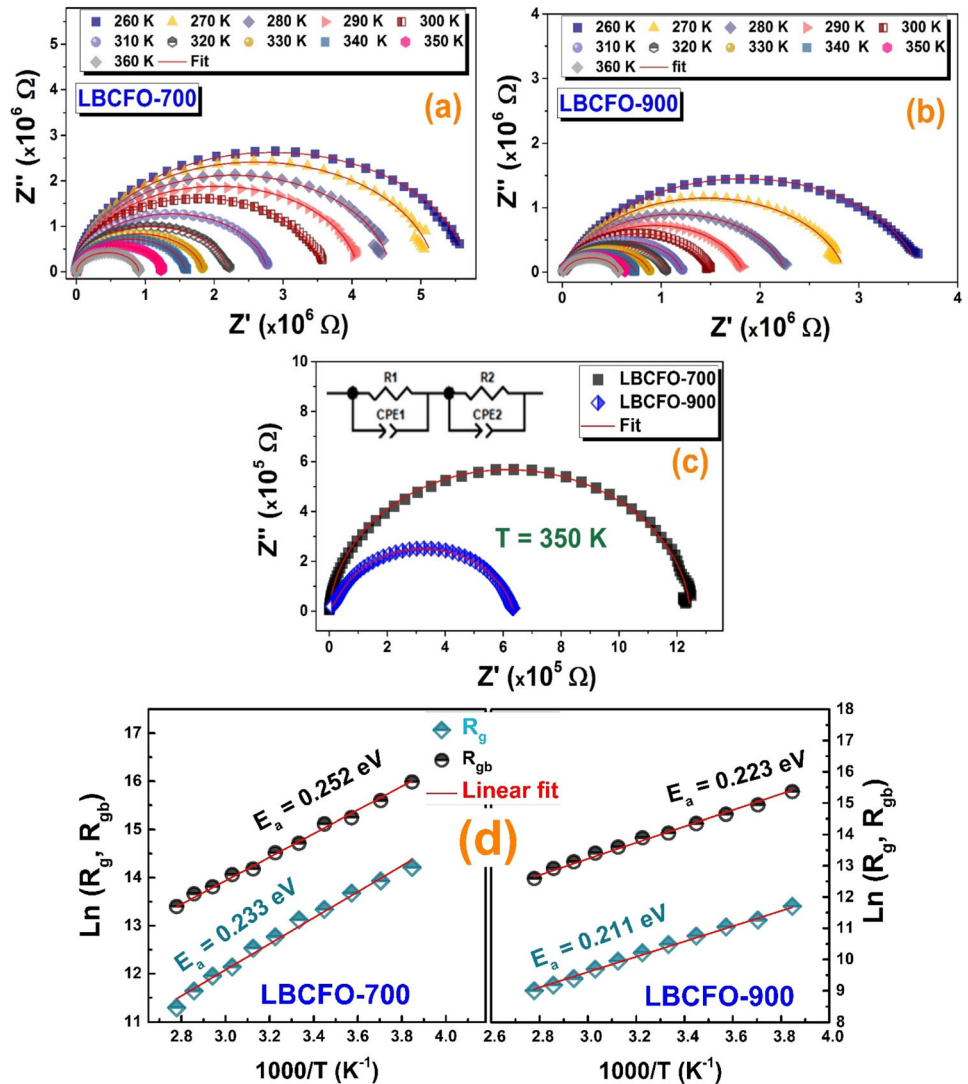
the used preparation method and the Cerium ions insertion in A-site for gas sensing applications of the Lanthanum ferrite system.

Moreover, the grain boundary resistance (R_{gb}) is higher than that of the grain (R_g). This can be explained by the presence of defects, for example the non-stoichiometric distribution of oxygen [42] near the grain boundaries. These defects act as traps for charge carriers at low temperatures. However, when the temperature increases, R_{gb} decreases and induces an augmentation in alternative conductivity σ_{ac}. As can also be seen, the values of α are close to the unit, which indicates that the CPE is very close to an ideal capacitor.

Furthermore, with the rise of the sintering temperature, the values of the grains and boundaries grains resistances were found to decrease. The logarithmic variation of the two resistances (R_g and R_{gb}) of the prepared compounds can be plotted as a function of $1000/T$ (Fig. 6d) and seems to follow the Arrhenius relation (shown by the red solid lines in Fig. 6d):

$$R = R_0 \exp\left(\frac{E_a}{k_B \times T}\right) \tag{3}$$

where R_0 is the characteristic resistance, k_B Boltzmann constant and E_a presents the activation energy. To estimate the activation energy of each contribution, we use the slope of the well-fitting curves and the values of the activation energies are summarized in Table 4. For the grain boundary contribution, the activation energies decrease from 0.252 to 0.223 eV with the increase in the heating temperature. Hence, the density of trapped carriers decreases when the

Table 3 Values of electrical parameters deduced from the complex diagram at selected temperatures for (a) LBCFO-700 and (b) LBCFO-900 compounds

T (K)	R_g ($\times 10^5$ Ω)	CPE$_1$ ($\times 10^{-10}$)	α_1	R_{bg} ($\times 10^6$ Ω)	CPE$_2$ ($\times 10^{-11}$)	α_2
(a)						
260	14.862	3.951	0.880	8.786	3.566	0.997
270	11.206	4.044	0.875	5.947	3.582	0.990
280	8.720	2.937	0.884	4.187	4.830	0.953
290	6.203	2.009	0.990	3.670	5.322	0.946
300	5.014	1.049	0.996	2.464	5.694	0.942
310	3.515	1.388	0.998	2.019	5.701	0.943
320	2.768	6.410	0.908	1.445	4.322	0.963
330	1.880	4.928	0.930	1.283	4.623	0.960
340	1.552	4.783	0.941	0.996	4.795	0.950
350	1.137	4.242	0.967	0.861	4.688	0.956
360	0.808	2.255	0.970	0.660	5.157	0.955

T (K)	R_g ($\times 10^4$ Ω)	CPE$_g$ ($\times 10^{-10}$)	α_1	R_{bg} ($\times 0^6$ Ω)	CPE$_{bg}$ ($\times 10^{-11}$)	α_2
(b)						
260	12.104	1.058	0.851	4.726	7.820	0.878
270	7.783	1.072	0.842	3.094	7.832	0.872
280	6.250	1.001	0.859	2.294	8.675	0.860
290	4.662	6.833	0.880	1.707	9.271	0.869
300	3.558	9.690	0.865	1.263	9.400	0.863
310	2.731	1.180	0.853	1.088	9.743	0.865
320	2.099	1.242	0.870	0.807	10.207	0.861
330	1.614	1.281	0.835	0.665	10.451	0862
340	1.197	1.388	0.847	0.503	10.700	0.868
350	0.970	1.473	0.860	0.407	10.411	0.850
360	0.809	1.404	0.850	0.295	10.780	0.861

**Table 4** Activation energy of our samples calculated from the different dielectric parameters

		LBCFO-700 E_a (eV)	LBCFO-900 E_a (eV)
Modulus (M'')	Grain contribution	–	0.208
	B. grain contribution	0.239	0.19
Impedance (Z'')	–	0.273	0.258
Nyquist (Z'' vs Z')	Grain contribution	0.233	0.211
	B. grain contribution	0.252	0.223

temperature increases, indicating the existence of a partial blocking of the free carrier movements by the grain boundaries, which affects the conductivity of the doped samples. the same behavior was also seen for grain contribution. For the contributions of both compounds, the activation energy values were found to strengthen the previous values and thus confirm the polaronic relaxation type throughout the studied compounds.

3.3 Dielectric constant ε'

The frequency dependence of the dielectric constant (ε') of the LBCFO-700 and LBCFO-900 compounds at selected temperature range are plotted in Fig. 7, showing that the highest values of the dielectric constant are at low-frequency region, which decreases with the increase in frequency. The variation in dielectric constant with frequency is explained on the basis of space charge polarization [43]. Furthermore, it has been confirmed that the existence of different Iron states rendered the pure and doped LaFeO$_3$

Fig. 7 Frequency dependence of the dielectric constant and the Kramers–Kronig transformed spectra (in inset) of the **a** LBCFO-700 and the **b** LBCFO-900 compounds
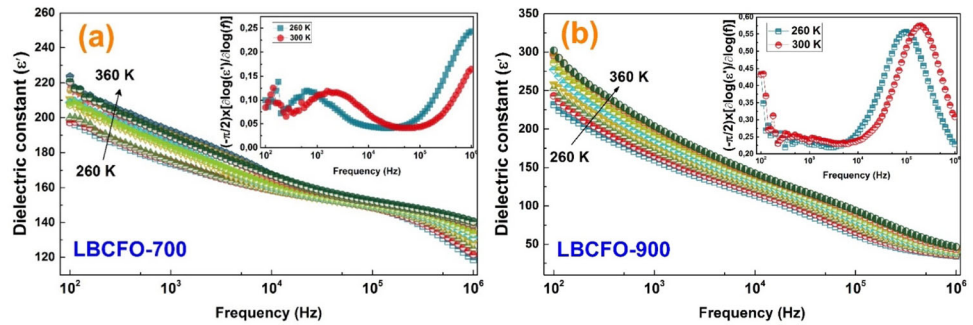
systems becomes dipolar [44]. At low frequencies, the high value of ε' in Lanthanum orthoferrite materials could be explained by the high ability of the permanent dipoles ($Fe^{2+} \leftrightarrow Fe^{3+}$) to align themselves along the field and contribute fully to the total polarization of the dielectric properties. Nevertheless, for higher frequencies, the almost constant values of ε' is due essentially to the inability of these dipoles to responds to the rapid variation of the applied field and therefore their contribution to the dielectric permittivity will be more negligible [45]. On the other hand, we noticed that the dielectric constant increases with the increase in temperature. This behavior can be explained by the fact that, with rising temperature, more dipoles will be oriented in the direction of the applied field, resulting in the increase of dipole moment value. It is to be noted that the dipole moment is the result of the rotation of dipoles when exposed to an external field [46].

It is also worthwhile to note that the bulk $LaFeO_3$ compound is known to present a giant dielectric constant (GDC), while in the present work, the dielectric constant of both compounds was found to be less than 300. It was confirmed that the growth of ferrite materials with the auto-combustion method reduces the dielectric constant due to the nanosize criteria induced by this preparation method. It has been confirmed by Bhat et al. that the maximum value of the dielectric constant of $LaFeO_3$ compound ($D_{SC} = 29.47$ nm) is around 120 [47]. Furthermore, the LBCFO-900 compound with higher particle size value presents a higher ε' value as compared to the LBCFO-700 compound, which confirms the effect of the particle size on the dielectric constant values and explains their low value in the studied compound compared to that of the bulk compound.

On the other hand, it has been confirmed that for highly conductive materials, the relaxation processes could be strongly masked by the conduction contribution. In such case, the logarithmic derivative of the permittivity part (known as the Kramers–Kronig transformation [48–50]) could be used to better analyze the relaxation processes. Therefore, the frequency derivatives were applied to the dielectric constant data of both LBCFO-700 and LBCFO-900 compounds and the results are shown in the inset of Fig. 7a, b, respectively. From the Kramers–Kronig transformed spectra, one can clearly see the presence of two relaxations peaks, indicating the presence of two different contributions in both compounds.

3.4 Modulus analysis

Based on the modulus analysis, we can further interpret the relaxation process and distinguish between the contributions throughout the studied nanomaterials. Figure 8a, b plots the frequency dependence of the imaginary part of the complex Modulus as a function of the frequency. For the LBBFO-700 compound, only one relaxation peak was observed at the selected temperature and frequency ranges. Yet, at high-frequency range, the M'' values continuously increased with frequency, proving the existence of other non-detected relaxation peaks. At the selected ranges, the LBCPFO-900 compound showed two distinguished relaxations peaks. For both compounds, while the low-frequency peaks are attributed to the grain boundary contribution, those appearing at high-frequency range are ascribed to the grain contribution. For a supplementary analysis of the relaxation phenomenon throughout both contributions, we adjusted the M'' curves according to the Bergman's function [51] (shown in solid red line in Fig. 8) expressed as follows:

$$M''(\omega) = \frac{M''_{max}}{(1-\beta) + \left(\frac{\beta}{1+\beta}\right)\left(\beta\left(\frac{f_{max}}{f}\right) + \left(\frac{f}{f_{max}}\right)^{\beta}\right)} \quad (4)$$

Fig. 8 Frequency dependence of the imaginary part of the Modulus (M'') at selected temperatures for our samples **a** LBCFO-700 and **b** LBCFO-900 compounds. **c** and **d** the Ln(f_{max}) vs. 1000/T of LCBFO-700 and LCBFO-900 compounds, respectively
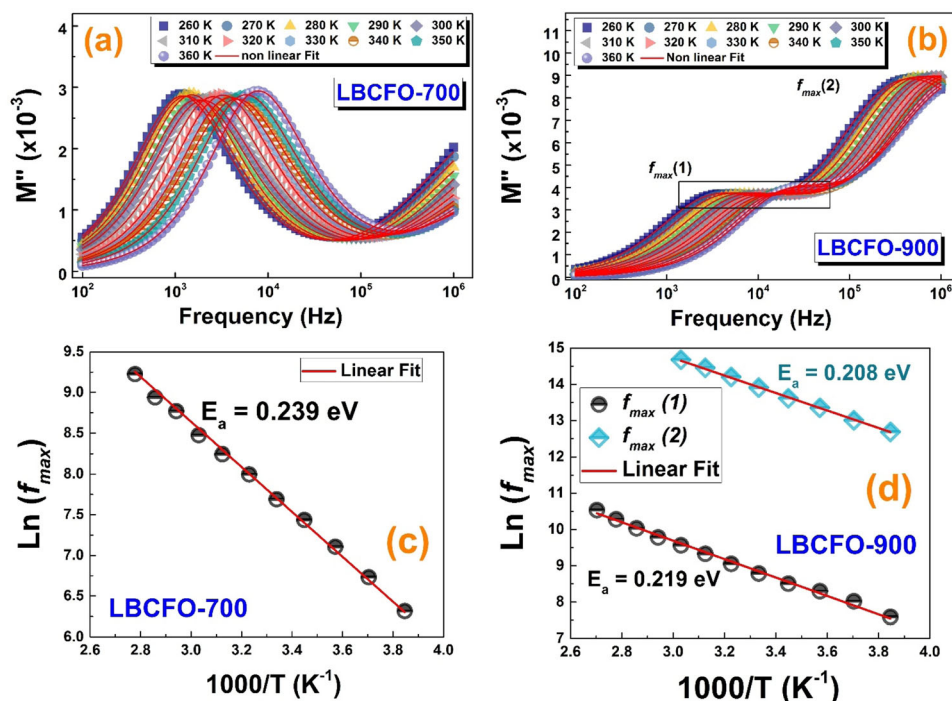
where M''_{max} is the peak maxima, β is the stretching factor (provides information about the kind of relaxation) and f_{max} is the corresponding frequency.

To calculate the activation energies of our samples, the relaxation frequency (f_{max}) obtained from the well fitted curves was used at selected temperatures. The variation of Ln(f_{max}) versus 1000/T is shown in Fig. 8c, d, and the calculated values of the activation energies are collected in Table 4. It is found that, all these values are quite similar to those calculated from impedance Nyquist.

3.5 AC electrical conductivity analysis

To determine the conduction behavior of our samples and the parameters which may control this process in our samples, we plotted the variation of the ac conductivity vs. frequency at selected temperatures. Hence, this study of electrical conductivity helps to envisage the effect of the annealing temperature on the conduction process.

As shown in Fig. 9a, b, two different regions are found as a function of the frequency. Actually, in the low-frequency range, a frequency-independent behavior is detected for both prepared compounds. This conductivity is considered as the dc conductivity that confirms the decrease of the resistance with the rise of temperature. In the higher region, the

conductivity increases with the rise of frequency, whose behavior (the frequency dependence of the conductivity) may emanate from the relaxation of the ionic atmosphere after the movement of the particle [52].

On the other hand, it is clear that the increase of the annealing temperature led to the increase in conductivity, which is deduced from the decrease in the resistance and confirmed from the frequency and temperature dependence of the ac conductivity, as shown in Fig. 9.

This increase in conductivity is likely to be related to the increase in particle size, which is accompanied by a decrease of the number of grain boundaries that acts as insulators, leading to the enhancement of the conductivity [53].

This variation is described by Jonscher's universal power law [54] expressed as:

$$\sigma_{ac}(\omega, T) = \sigma_{dc} + A\omega^{S(T)} \tag{5}$$

In the last expression, σ_{dc} is the dc conductivity, A is a constant depending on temperature, which determines the strength of polarizability, and the exponent S is the frequency exponent, which depends on temperature and the material intrinsic property, informs about the degree of interaction between mobile ions with the lattices around them. The spectrums of the conductivity at the high-

Fig. 9 Variation of the ac conductivity as a function of the frequency at selected temperatures of the **a** LBCFO-700 and **b** LBCFO-900 samples. **c** the temperature dependence of the S parameter for both samples with the corresponding binding energy of the carrier values
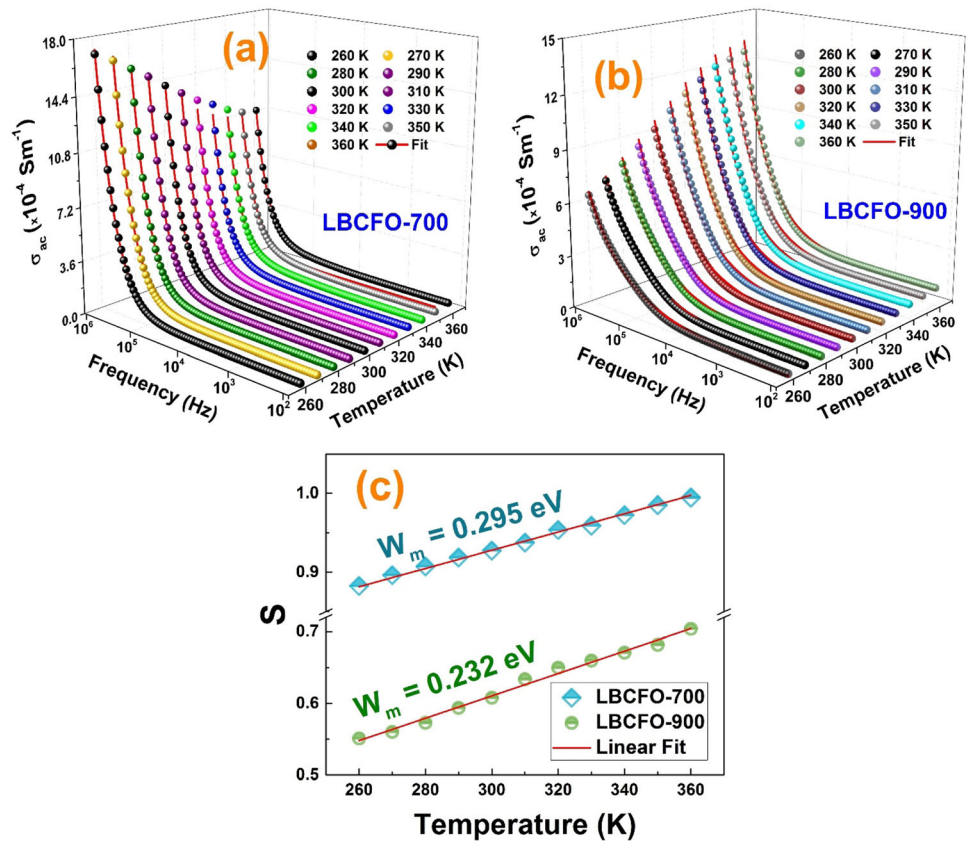
frequency range are well fitted using Eq. (3), and the values of σ_{dc}, S and A calculated from the adjusted results of the conductivity plots are summarized in Tables 5(a) and (b). The conduction mechanism has been confirmed by the analysis of $S(T)$ curves, related to Fence [55]: when $S \leq 1$: the load carriers have a translational movement and when $S > 1$: there is a localized jump of the carriers.

To determine the mechanism of conduction in our compounds, the values of S are plotted against the temperature as shown in Fig. 9c, from which it is clearly seen that for both compounds the Jonscher's power law parameter 'S' increases with the increase in temperature. What is worthy to mention that, based on the behavior of Jonscher's power law parameter S, the conduction mechanism within the material can be one of the following models:

i. *The model of Quantum Mechanical Tunneling (QMT) model where S is around 0.8 and found to be independent to temperature [56].*

ii. *The model of Correlated Barrier Hopping (CBH) model where the exponent S decreases with the rise of temperature [57].*

iii. *The Non-overlapping Small Polaron Tunneling (NSPT) model where S increases with the increase in temperature [58].*

iv. *The model of Overlapping Large Polaron Tunneling (OLPT) S decreases and then increases with the rise of temperature [59].*

Accordingly, given that the exponent S increases with the increase in temperature for both compounds, the NSPT is the appropriate model to be used when describing the conduction mechanism of both compounds.

It is trusty to note that for this model, the temperature dependence of the S parameter can be expressed as follows [58]:

$$S = 1 + \frac{4k_B T}{W_m - k_B T \ln(\omega \tau_0)} \tag{6}$$

where W_m is a binding energy of the carrier, k_B the Boltzmann's constant and τ_0 is a characteristic relaxation time.

For the large value of $\left(\frac{W_M}{k_B T}\right)$ the equation of S becomes:

Table 5 Parameters (dc conductivity, temperature-dependent factor (A), and exponent (S)) obtained using the data fitted following the Jonscher's power law for (a) LBCFO-700 and (b) LBCFO-900 compounds

T (K)	σ_{dc} ($\times 10^{-5}$)	A ($\times 10^{-12}$)	S
(a)			
260	0.970	22.390	0.882
270	0.929	12.451	0.896
280	1.200	6.463	0.907
290	1.381	5.441	0.918
300	1.784	2.580	0.927
310	2.491	2.254	0.937
320	3.201	2.101	0.953
330	3.433	2.160	0.959
340	4.751	1.798	0.972
350	5.520	1.806	0.985
360	7.764	1.584	0.994
(b)			
260	0.977	2.383	0.551
270	0.929	2.253	0.560
280	1.290	2.040	0.573
290	1.660	1.745	0.593
300	1.921	1.465	0.608
310	2.165	1.272	0.634
320	3.100	0.882	0.650
330	3.291	0.680	0.662
340	4.597	0.521	0.671
350	5.720	0.420	0.682
360	7.191	0.349	0.704

$$S = 1 + \frac{4k_B T}{W_m} \tag{7}$$

The W_m values were calculated from the slope of a linear adjustment of the deduced $S(T)$ curves as shown in Fig. 9c. It is deduced that the increase of the sintering temperature has an effect on the binding energy. Actually, the LBCFO-700 compound was found to have lower values compared to the same compound heated at 900 °C.

4 Conclusion

The $La_{0.8}Ba_{0.1}Ce_{0.1}FeO_3$ (LBCFO) ferrite material was successfully synthesized by the sol–gel auto-combustion route and the obtained nanoparticles were treated separately at two different annealing temperatures, namely 700 °C and 900 °C. The microstructure, dielectric relaxation and conduction mechanism of synthesis compounds showed a dependence on the heat treatment. Both compounds exhibited pure and single perovskite phase with orthorhombic structure. The XRD and TEM analyses revealed that the average crystallite sizes increase with the increase in the annealing temperature in the range of 50–70 nm. It has been found that the relaxation process is of a polaronic type that occurring separately in grain and boundary grains contributions with activation energies that decrease with the increase in the annealing temperature. The conduction mechanism in both compounds is attributed to the jump of polarons between Iron states. The electrical resistance was found to decrease with the increase in the annealing temperature, consequently leading to a rise in conductivity. It can be concluded that the auto-combustion synthesis method with 900 °C annealing temperature of such materials would enhance their gas sensing properties.

References

1. A. Schön, C. Dujardin, J.P. Dacquin, P. Granger, Enhancing catalytic activity of perovskite-based catalysts in three-way catalysis by surface composition optimization. Catal. Today **258**, 543–548 (2015)

2. H. Tanaka, I. Tan, M. Uenishi, M. Taniguchi, M. Kimura, Y. Nishihata, J. Mizuki, LaFePdO₃ perovskite automotive catalyst having a self-regenerative function. J. Alloys Compd. **408–412**, 1071–1077 (2006)

3. Y. Wang, A. Zhu, B. Chen, M. Crocker, C. Shi, Three-dimensional ordered mesoporous Co–Mn oxide: a highly active catalyst for "storage–oxidation" cycling for the removal of formaldehyde. Catal. Commun. **36**, 52–57 (2013)

4. X.P. Dai, Q. Wu, R.J. Li, C.C. Yu, Z.P. Hao, Hydrogen production from a combination of the water−gas shift and redox cycle process of methane partial oxidation via lattice oxygen

over LaFeO₃ perovskite catalyst. J. Phys. Chem. B **110**, 25856–25862 (2006)

5. H. Chen, S. Yang, Carbon-based perovskite solar cells without hole transport materials: the front runner to the market. Adv. Mater. **24**, 1603994 (2017)

6. V.M. Gaikwad, S.A. Acharya, Novel perovskite–spinel composite approach to enhance the magnetization of LaFeO₃. RSC Adv. **5**, 14366 (2015)

7. D. Wang, M. Gong, Surface and shape anisotropy effects in LaFeO₃ nanoparticles. J. Appl. Phys. **109**, 114304 (2011)

8. M. Viret, D. Rubi, D. Colson, D. Lebeugle, A. Forget, P. Bonville, G. Dhalenne, R. Saint-Martin, G. André, F. Ott, β-NaFeO₂, a new room-temperature multiferroic material. Mater. Res. Bull. **47**, 2294–2298 (2012)

9. W.G. Wang, M. Mogensen, High-performance lanthanum-ferrite-based cathode for SOFC. Solid State Ion. **176**, 457 (2005)

10. Y. Pei, Y. Li, J.Y. Che, W. Shen, Y. Wang, S. Yang, S. Han, Study on the high-temperature electrochemical performance of perovskite-type oxide LaFeO₃ with carbon modification. Int. J. Hydrogen Energy **40**, 8742–8749 (2015)

11. P. Xiao, L. Zhong, J. Zhu, J. Hong, J. Li, H. Li, Y. Zhu, CO and soot oxidation over macroporous perovskite LaFeO₃. Catal. Today **258**, 660–667 (2015)

12. H. Zhang, H. Qin, C. Gao, G. Zhou, Y. Chen, J. Hu, UV light illumination can improve the sensing properties of LaFeO₃ to acetone vapor. Sensors **18**, 1990 (2018)

13. N. Afifah, R. Saleh, The influence of TiO₂ nanoparticles on LaFeO₃/TiO₂ nanocomposites for reduction of aqueous organic dyes. J. Phys. Conf. Ser. **1788**, 030080 (2017)

14. J.A. Gómez-Cuaspud, E. Vera-López, J.B. Carda-Castelló, E. Barrachina-Albert, One-step hydrothermal synthesis of LaFeO₃ perovskite for methane steam reforming. Reac. Kinet. Mech. Cat. **120**, 167–179 (2017)

15. M. Idrees, M. Nadeem, S.A. Siddiqi, R. Ahmad, A. Hussnain, M. Mehmood, The organic residue and synthesis of LaFeO₃ by combustion of citrate and nitrate precursors. Mater. Chem. Phys. **162**, 652–658 (2015)

16. M. Idrees, M. Nadeem, M.M. Hassan, Investigation of conduction and relaxation phenomena in LaFe0.9Ni0.1O3 by impedance spectroscopy. J. Phys. D **43**, 15 (2010)

17. E. Cao, Y. Qin, T. Cui, L. Sun, W. Hao, Y. Zhang, Influence of Na doping on the magnetic properties of LaFeO3 powders and dielectric properties of LaFeO₃ ceramics prepared by citric sol-gel method. Ceram. Int. **43**, 7922–7928 (2017)

18. S. Phokha, S. Hunpratup, S. Pinitsoontorn, B. Pustasaeng, S. Rujirawat, S. Maensiri, Structure, magnetic, and dielectric properties of Ti-doped LaFeO₃ ceramics synthesized by polymer pyrolysis method. Mater. Res. Bull. **67**, 118–125 (2015)

19. L. Sun, H. Qin, K. Wang, M. Zhao, J. Hu, Structure and electrical properties of nanocrystalline La₁₋ₓBaₓFeO₃ for gas sensing application. Mater. Chem. Phys. **125**, 305–308 (2011)

20. X.P. Xiang, L.H. Zhao, B.T. Teng, J.J. Lang, X. Hu, T. Li, Y.A. Fang, M.F. Luo, J.J. Lin, Catalytic combustion of methane on La₁₋ₓCeₓFeO₃ oxides. Appl. Surf. Sci **276**, 328–332 (2013)

21 F.B. Abdallah, A. Benali, S. Azizi, M. Triki, E. Dhahri, M.P.F. Graça, M.A. Valente, Strontium-substituted La₀.₇₅Ba₀.₂₅₋ₓ-SrₓFeO₃ (x = 0.05, 0.10 and 0.15) perovskite: dielectric and electrical studies. J. Mater. Sci. **30**, 8457–8470 (2019)

22 F.B. Abdallah, A. Benali, M. Triki, E. Dhahri, K. Nomenyo, G. Lerondel, Investigation of structural, morphological, optical and electrical properties of double-doping Lanthanum ferrite. J. Mater. Sci. **30**, 3349–3358 (2019)

23. A. Benali, S. Azizi, M. Bejar, E. Dhahri, M.F.P. Graça, Structural, electrical and ethanol sensing properties of double-doping LaFeO₃ perovskite oxides. Ceram. Int. **40**, 14367–14373 (2014)

24. E.M. Benali, A. Benali, M. Bejar, E. Dhahri, M.P.F. Graca, M.A. Valente, B.F.O. Costa, J. Mater. Sci. **31**, 3197–3214 (2020)

25. C. Zhu, A. Nobuta, I. Nakatsugawa, T. Akiyama, Solution combustion synthesis of LaMO3 (M= Fe Co, Mn) perovskite nanoparticles and the measurement of their electrocatalytic properties for air cathode. Int. J. Hydrogen Energy **38**, 13238 (2013)

26. R.A. Young, *The Rietveld Method* (Oxford University Press, New York, 1993)

27. Z. Dai, C.-S. Lee, B.-Y. Kim, C.-H. Kwak, J.-W. Yoon, H.-M. Jeong, J.-H. Lee, Honeycomb-like periodic porous LaFeO3 thin film chemiresistors with enhanced gas-sensing performances. ACS Appl. Mater. Interfaces **2014**(6), 16217–16226 (2018)

28. N. Karthikeyan, R. Ramesh Kumar, G. Jaiganesh, K. Sivakumar, Thermoelectric power factor of La0.9M0.1FeO3 (M ¼ Ca and Ba) system: Structural, band gap and electrical transport evaluations. Phys. B **529**, 1–8 (2018)

29. M. Idrees, M. Nadeem, M. Shah, T.J. Shin, Anomalous octahedral distortions in LaFe1−xNixO3. J. Phys. D **44**, 1–8 (2011)

30. N.S. Goncalves, J.A. Carvalho, Z.M. Lima, J.M. Sasaki, Size–strain study of NiO nanoparticles by X-ray powder diffraction line broadening. Mater. Lett. **72**, 36–38 (2012)

31. W. Ncib, A.B.J. Kharrat, M. Saadi, K. Khirouni, N. Chniba-Boudjada, W. Boujelben, Structural, AC conductivity, conduction mechanism and dielectric properties of La₀.₆₂Eu₀.₀₅-Ba₀.₃₃Mn₀.₈₅Fe₀.₁₅O₃ ceramic compound. J. Mater. Sci. **30**, 18391–18404 (2019)

32. A.R. James, K. Srinivas, Low temperature fabrication and impedance spectroscopy of PMN-PT ceramics. Mater. Res. Bull. **34**, 1301 (1999)

33. H. Baaziz, N.K. Maaloul, A. Tozri, H. Rahmouni, S. Mizouri, K. Khirouni, E. Dhahri, Effect of sintering temperature and grain size on the electrical transport properties of $La_{0.67}$-$Sr_{0.33}MnO_3$ manganite. Chem. Phys. Lett. **640**, 77 (2015)

34. S. Hcini, A. Selmi, H. Rahmouni, A. Omri, M.L. Bouazizi, Polaronic relaxation in $LaFeO_3$, Structural, dielectric and complex impedance properties of $T_{0.6}Co_{0.4}Fe_2O_4$ (T= Ni, Mg) ferrite nanoparticles prepared by sol gel method. Ceram. Int. **43**, 2529 (2017)

35. C. Chen, K.B. Xu, Y.M. Cui, C.C. Wang, Polaronic relaxation in $LaFeO_3$. Mater. Lett. **89**, 153–155 (2012)

36. T.L. Rao, M.K. Pradhan, M. Chandrasekhar, P.V. Ramakrishna, S. Dash, J. Phys. **31**, 345803–345814 (2019)

37. D. Johnson, Z. Plot, Z-View Electrochemical Impedance Software, Version 2.3b (Scribner Associates, Inc., North Carolina, 2000)**.**

38. H. Trabelsi, M. Bejar, E. Dhahri, M. Sajieddine, K. Khirouni, P.R. Prezas, B.M.G. Melo, M.A. Valente, M.P.F. Garça, Effect of oxygen vacancies on $SrTiO_3$ electrical properties. J. Alloys Compd. **723**, 894–903 (2017)

39. S.M. Khetre, H.V. Jadhav, P.N. Jagadale, S.R. Kulal, S.R. Bamane, Studies on electrical and dielectric properties of $LaFeO_3$. Adv. Appl. Sci. Res **2**(4), 503–511 (2011)

40. P.B. Koli, K.H. Kapadnis, U.G. Deshpande, Methanol gas sensing properties of pervoskite $LaFeO_3$ nanoparticles doped by transition metals Cr3+ and Co2+. J. Chem. Pharm. Res. **9**, 253–259 (2017)

41. L. Suna, H. Qina, K. Wangb, M. Zhaoa, J. Hua, Structure and electrical properties of nanocrystalline $La1-xBaxFeO3$ for gas sensing application. Mater. Chem. Phys. **125**, 305–308 (2011)

42. M. Khelifi, R. M'nassri, A. Selmi, H. Rahmouni, K. Khirouni, N. Chniba Boudjada, A. Cheikhrouhou, Investigation of magnetic and transport properties of PrCa(MnCo)O prepared by solid state process. J. Magn. Magn. Mater. **423**, 20–26 (2017)

43. C.W. Wu, Y.H. Nan, Y. Lin, Deng, Giant dielectric permittivity observed in Li and Ti doped NiO. Phys. Rev. Lett. **89**, 217601 (2002)

44. G. Gowri, R. Saravanan, S. Sasikumar, I.B. Shameem Banu, Exchange bias effect, ferroelectric property, primary bonding and charge density analysis of $La1-xCexFeO3$ multiferroics. Mater. Res. Bull. **118**, 110512 (2019)

45. M. Idrees, M. Nadeem, M. Mehmood, M. Atif, K.H. Chae, M.M. Hassan, Impedance spectroscopic investigation of delocalization effects of disorder induced by Ni doping in $LaFeO3$. Acta Mater. **44**, 105401 (2011)

46. G.R. Hearne, M.P. Pasternak, R.D. Taylor, P. Lacorre, Electronic structure and magnetic properties of $LaFeO3$ at high pressure. Phys. Rev. B **51**, 11495–11500 (1995)

47. I. Bhat, S. Husain, W. Khan, S.I. Patil, Effect of Zn doping on structural, magnetic and dielectric properties of $LaFeO3$ synthesized through sol–gel auto-combustion process. Mater. Res. Bull. **48**, 4506–4512 (2013)

48. A. Sieradzki, S. Pawlus, S.N. Tripathy, A. Gągor, M. Ptak, M. Paluch, M. Mączka, Dielectric relaxation and anhydrous proton conduction in [C2H5NH3][Na0.5Fe0.5(HCOO)3] metal-organic framework. Dalton Trans. **46**, 3681–3687 (2017)

49. A. Molak, M. Paluch, S. Pawlus, J. Klimontko, Z. Ujma, I. Gruszka, J. Phys. D **38**, 1450–1460 (2005)

50. M. Wubbenhorst, J. Van Turnhout, J. Non-Cryst, Solids **305**, 40–49 (2002)

51. R. Bergman, General susceptibility functions for relaxations in disordered systems. J. Appl. Phys. **88**, 1356 (2000)

52 E. Barsoukov, J.R. Macdonald, *Impedance Spectroscopy Theory, Experiment and Applications*, 2nd edn. (Wiley, New York, 2005)

53. S. Mazen, N.I. Abu-Elsaad, Structural, magnetic and electrical properties of the lithium ferrite obtained by ball milling and heat treatment. Appl. Nanosci. **5**, 105–114 (2015)

54. A.K. Jonscher, *Universal Relaxation Law* (Chelsea Dielectric Press, London, 1996)

55. K. Funke, Jump relaxation in solid electrolytes. Prog. Solid State Chem. **22**, 111–195 (1993)

56. M. Pollak, On the frequency dependence of conductivity in amorphous solids. Philos. Mag. **23**, 519–542 (1971)

57. S. Mollah, K.K. Som, K. Bose, B.K. Chaudhuri, Ac conductivity in Bi4Sr3Ca3CuyOx (y=0–5) and Bi4Sr3Ca3−−zLizCu4Ox (z=0.1–1.0) semiconducting oxide glasses. J. Appl. Phys. **74**, 931 (1993)

58. A. Ghosh, Frequency-dependent conductivity in bismuth-vanadate glassy semiconductors. Phys. Rev. B **41**, 1479 (1990)

59. M. Megdiche, C. Perrin-Pellegrino, M. Gargouri, Conduction mechanism study by overlapping large-polaron tunnelling model in $SrNiP_2O_7$ ceramic compound. J. Alloys Compd. **584**, 209–215 (2014)